Histologic Photoreceptor and Retinal Pigment Epithelium Degeneration in an Eye With Clinically Documented Geographic Atrophy of AMD

Christine A. Curcio,[1] Jeffrey D. Messinger,[1] Kenneth R. Sloan,[2] Malia M. Edwards,[3] Jacques Bijon,[4] Florentin Huemer,[5] Oliver Leingang,[5] K. Bailey Freund,[4,6] and Andreas Berlin[1,7]

[1]Department of Ophthalmology and Visual Sciences, Heersink School of Medicine, University of Alabama at Birmingham, Birmingham, Alabama, United States
[2]Department of Computer Science, University of Alabama at Birmingham, Birmingham, Alabama, United States
[3]Wilmer Eye Institute, Johns Hopkins University, Baltimore, Maryland, United States
[4]Vitreous Retina Macula Consultants of New York, New York, New York, United States
[5]RetinSight, Vienna, Austria
[6]Department of Ophthalmology, New York University Grossman School of Medicine, New York, New York, United States
[7]Department of Ophthalmology, University Hospital Würzburg, Würzburg, Germany

Correspondence: Christine A. Curcio, Department of Ophthalmology and Visual Sciences, 1670 University Boulevard Room 353, University of Alabama at Birmingham, School of Medicine, Birmingham, AL 35294-0019, USA; cacurcio@gmail.com.

Received: October 20, 2025
Accepted: March 15, 2026
Published: April 7, 2026

Citation: Curcio CA, Messinger JD, Sloan KR, et al. Histologic photoreceptor and retinal pigment epithelium degeneration in an eye with clinically documented geographic atrophy of AMD. *Invest Ophthalmol Vis Sci.* 2026;67(4):12. https://doi.org/10.1167/iovs.67.4.12

Purpose. In geographic atrophy (GA) of AMD, comparing photoreceptor disintegrity and RPE loss in optical coherence tomography (OCT) and microscopy may elucidate atrophy expansion and suggest imaging biomarkers.

Methods. One eye of a 93-year-old woman with bilateral drusen-driven GA of AMD was analyzed. RPE loss and reduced photoreceptor segment integrity (rPSi) was quantified automatically in clinical OCT volumes over a five-year period ending six years pre-mortem. In transmission electron micrographs of the outer junctional zone (OJZ) and a comparison area, tissue component volumes were measured.

Results. By OCT, rPSi area exceeded RPE loss at baseline. Yearly RPE loss (2.432 mm^2) exceeded rPSi (1.770 mm^2) as these areas converged. By microscopy, the mean distance between the external limiting membrane (ELM) and RPE basal lamina in the OJZ was 50% of the comparison. Volumes of interphotoreceptor space, outer segments, inner segment myoids, inner segment ellipsoids, and in-layer RPE were 16%, 17%, 25%, 50%, and 104%, respectively, of the comparison. Cone inner segments exhibited fragmented and translocating mitochondria over drusen and at the ELM descent. In some OCT scans, the descent appeared especially hyperreflective.

Conclusions. In this first clinicopathologic correlation of an AMD eye with a known GA growth rate, the area of rPSi (a composite representing photoreceptor shortening, disorganization, altered waveguiding, and true cell death) exceeds the area of RPE loss. The OJZ exhibits dysmorphic but continuous RPE. Photoreceptors degenerate from the outer segments inward. Mitochondrial fission and translocation at the ELM descent may be visible clinically.

Keywords: age-related macular degeneration, geographic atrophy, optical coherence tomography, deep learning trained OCT-based segmentation, histopathology, drusen, cones, rods, retinal pigment epithelium, growth rate, transmission electron microscopy

Geographic atrophy (GA), the end-stage of nonexudative AMD, includes loss of photoreceptors, RPE, and choriocapillaris, in the setting of stereotypic extracellular deposits. This pathology is visible in remarkable detail with contemporary multimodal clinical imaging.[1–3] Retarding atrophy expansion as revealed by fundus autofluorescence was the regulatory endpoint met by US-approved complement inhibitors for treating GA.[4,5] Automated approaches to quantifying atrophy are enabled by optical coherence tomography (OCT). Herein we address the histologic basis of these OCT-based methods.

Development of new AMD therapies hinges on imaging outcome measures for photoreceptor health that credibly substitute for visual function tests. Measures involving photoreceptor-involving OCT bands like ellipsoid zone (EZ) must consider aspects of degeneration uncovered or newly appreciated in recent research. In AMD eyes, photoreceptors that are shortened or deflected by deposits in histology[6] may be present but poorly visible by OCT and adaptive optics scanning laser ophthalmoscopy.[7] EZ visibility depends on the direction of incoming light.[8] Thus, poor visibility may signify cellular abnormality but not necessarily cell death.

Furthermore, EZ visibility can reconstitute spontaneously during AMD evolution[9–11] or improve after an intervention.[12]

Because existing GA enlarges via cellular interactions at the margins, microscopic observations of GA eyes are relevant. The termination of a continuous RPE layer is considered the GA border by biomicroscopy and color fundus photography. Histology and OCT have revealed another border in the neurosensory retina, the descent of the external limiting membrane (ELMd) toward Bruch's membrane (BrM). The ELMd divides an outer junctional zone (OJZ),[13] containing potentially salvageable photoreceptors, from areas of near-total photoreceptor depletion.[14–16] The ELMd and OJZ are most readily conceptualized as surrounding a single large area (unifocal GA). However, each of the small atrophic spots that begin atop individual drusen is also bounded by an ELMd and OJZ (multifocal GA).[17] Over time, these spots expand and merge.[17]

Post-hoc analyses of clinical trial OCT data showed that the area of affected photoreceptors (i.e., in the OJZ) exceeded that of RPE loss at all time points, and that treatment decelerated expansion of "EZ loss" more than RPE.[18,19] Furthermore, eyes with larger "EZ loss" than RPE loss exhibited faster progression than eyes with similar areas.[20] Algorithms to recognize GA features in OCT were separately trained with different deep-learning techniques (single and ensemble convolutional neural nets, for RPE and photoreceptors, respectively).[21–23] Areas of RPE loss in OCT correlated with atrophy in fundus autofluorescence (Pearson r, 0.97).[24] Photoreceptor status was expressed as axial distances between inner boundaries of the EZ and the RPE–BrM band; distances ≤4 µm were called EZ loss. Algorithm training material included eyes with exudative disease[25] and GA cases including trial participants.[23,26]

Clinicopathologic correlation, i.e., histology of eyes imaged during life, can validate diagnostic technology with anatomic ground truth and probe disease pathophysiology. Classic microscopy studies offered binary judgments about photoreceptor presence yet neither quantified rates of RPE and photoreceptor degeneration nor compared the OJZ to less-affected areas in the same eyes.[27] To fill these gaps, transmission electron microscopy (TEM) is suitable because it comprehensively reveals tissue ultrastructure, including lipid-aqueous interfaces that generate OCT reflectivity. We recently reported a histologic analysis of an eye with multifocal GA and five years of OCT and fundus autofluorescence imaging.[17] In this same index eye, we now report automatically quantified growth rates for areas of RPE atrophy and photoreceptor abnormality. We compare ultrastructure of the OJZ to less-affected retina. Finally, we offer initial observations of presumed mitochondrial fission at the ELMd, building on our previous descriptions of outer retinal tubulation (ORT) in AMD.[28,29]

Methods

Compliance

Retrospective review of medical records and imaging data and the histopathologic study were approved by institutional review boards of the Manhattan Eye, Ear, and Throat Hospital/Northwell Health and the University of Alabama at Birmingham, respectively. This study was conducted in accordance with the Declaration of Helsinki and the Health Insurance Portability and Accountability Act of 1996.

Clinical Course and Clinical Imaging

The clinical course and imaging parameters were previously described[17] and are available in the Supplementary Material S1. An 82-year-old Caucasian woman was monitored over a five-year period for bilateral multifocal GA secondary to AMD, with many drusen, some subretinal drusenoid deposits, and lacking neovascularization. At the last registered clinical evaluation, five years after presentation and six years before death, BCVA was 20/400 and 20/100 in the right and left eyes, respectively. The patient died of breast cancer at age 93 years.

Automatic Measurement of Atrophy Area and Growth Rate by OCT

To detect, delineate, and quantify photoreceptor degeneration and RPE loss, structural B-scans within 6 × 6 mm square OCT volumes were segmented automatically. The segmentation algorithms are CE-marked, proprietary convolutional neural network–based (U–Net–style) (GA Monitor, next-generation unreleased version 2.1 as presented at ARVO 2025; Vogl et al.[22] https://iovs.arvojournals.org/article.aspx?articleid=2803744; RetInSight, Vienna, Austria).[21,25,30] Three OCT volumes with the most scans (49 scans at 11 years premortem, 31 scans at nine years, and 31 scans at six years) that met requirements of the algorithm were submitted for analysis. These were six fovea-centered, horizontal 30° × 20° (nominally 9 × 6 mm) scan patterns with a resolution of 1536 × 496 pixels per B-scan, on a Spectralis platform. The standard analysis reports provided maps of photoceptor degeneration and RPE loss within 1-mm and 6-mm diameter zones. To meet the input constraints of the deep-learning model, each OCT volume was cropped to a 6 × 6 mm (≈20° × 20°) macular field. The 9 × 6 mm field of view of the raw scan was thus cropped to a 6 × 6 mm square before analysis, and the 6 × 6 mm full field of view en face square was derived in addition to the standard report outputs. This restricted field of view may censor borders of photoreceptor degeneration and exclude extensions beyond the field of view, biasing downward the estimated expansion in photoreceptor invisibility, in total. Segmentations were manually reviewed for accuracy by a computer scientist (author O.L.) experienced in retinal imaging and biomarker annotation.

Terminology

"EZ loss" reported by GA Monitor is based on research by the Schmidt-Erfurth[19] and Guymer[31] groups. "EZ loss" is defined as axial distance ≤4 µm between inner boundaries of the EZ and RPE-BrM bands, equivalent to a single pixel. Because of histologic and optical considerations (details in Discussion), herein we call EZ loss "reduced photoreceptor segment integrity" (rPSi). The term "photoreceptor segment"[32] was adopted because the measured OCT distance includes both inner and outer segments (OS)—and possibly also a thin hyporeflective band in the inner RPE cell bodies.[33,34]

In contrast, we adhere to the term "RPE loss" as reported by GA Monitor. This is indicated by the complete absence of RPE in combination with hypertransmission in the underlying choroid, without minimum size requirements. We consider "RPE loss" appropriate, because of the high correlation of OCT and fundus autofluorescence measures of atrophy.[24] Furthermore, imaging and histology indicate few cells with RPE-originated organelles scat-

tered in the atrophic area.[35–37] They are expected to have little impact on global measures of autofluorescence intensity.

For descriptive purposes only and for comparison to histology, two morphologic patterns of ELMd were distinguished on structural OCT B scans of the index eye: a typical thin ELM and a thickened and hyperreflective type. ELMd was classified by expert review (authors C.C, K.B.F.) based on predefined qualitative and semiquantitative criteria (details in Supplementary Materials S1). This exploration did not involve automated analysis.

Overview of Laboratory Studies

Tissue preparation for the index eye of this report (OS)[17] is described in Supplementary Materials S1. Herein we emphasize the bilaterality and symmetry of multifocal GA in the two eyes, atrophy growth rates of both eyes, and OCT features appearing in both eyes. The fellow eye (OD) was preserved in a different fixative that allowed analyses using labeling techniques that were less possible with the electron microscopy fixative used for the index eye (OS). In brief, analysis of the neurosensory retina (OD) illuminated the extensive activity of Müller glia in the atrophic area.[38] Analysis of the choroid (OD) illuminated macro- and microvasculature pathology and a neovascular complex outside the central area.[39]

Quantification of Tissue Compartments in the Index Eye

For ultrastructural analysis, the OJZ was operationally defined as a 500 µm strip starting at the ELMd and heading outwardly along BrM. Our prior studies of atrophy[15,40,41] predated the OJZ term[13] but established that abnormal RPE and photoreceptor morphologies increase in a cascading process within 500 µm of the ELMd.[15,27,40,42–46] Herein we compared OJZ between fovea and optic nerve head to a less-involved comparison area temporal to the main atrophy in the same tissue block. Both OJZ and comparison areas lie outside the ETDRS grid and are very rod-dominant.[47] Imaging and histology correlations were based on representative findings rather than point-to-point comparisons. Several factors prevented a precise match of histology and OCT findings of RPE or photoreceptor loss at specific locations. These were the six-year gap between the last clinical visit and death, tissue- and section-level artifacts (detachment and shattering, respectively), and the limited number of samples saved for TEM.

Our ultrastructure metric was volume (mm^3) occupied by tissue components between the ELM and the RPE basal lamina (BL), in the OJZ and comparison area. To determine these values and provide quality control, we evaluated all the tissue components between the ELM and the inner collagenous layer of BrM, in two steps. First, percent volume occupancies of tissue components were measured using point-counting stereology. Second, percentages were converted to volumes (mm^3) with information about total tissue volume. Use of percentages assumes that shrinkage caused by tissue preparation is uniform across tissue components, which is reasonable considering that extracellular matrix was largely excluded.

Point-counting stereology comprises superimposing a systematic sample of grid points on an image and scoring the image component under each point.[48] The proportion of points scored for any one component, relative to total points, is an unbiased estimator of volume occupancy. For example, if 100 points are placed on an electron micrograph, and 10 overlie inner segment myoid (ISmy), then the volume occupancy of ISmy is 10%.

We updated custom FIJI software[49] for guided point-counting stereology[50] (workflow and access information in Supplementary Material S2). The software accepts an image, a list of allowable tissue categories, and grid spacing (set at 10 µm). It displays one point at a time for scoring by an operator with a keypad, displays all scored points as a color-coded grid (Supplementary Fig. 2), and writes a .tsv output file. Allowable tissue components included ELM; ISmy; inner segment ellipsoid (ISel); OS; interphotoreceptor space (IPS, occupied in vivo by interphotoreceptor matrix); subretinal drusenoid deposit (SDD); Sloughed RPE[35] (cells organelles in the subretinal space with numerous RPE-specific); layer of RPE cell bodies; RPE granule aggregates within basal laminar deposit (BLamD); BLamD; basal linear deposit /drusen; calcified drusen; Other Cell Type; Empty Space in Tissue (due to preparation artifact), and Indeterminate.

Volume occupancies were converted to volumes (mm^3) by multiplying the percentages by a volume. The volume was a unit area (1 mm^2) times the mean distance between the ELM and RPE-BL. This distance was measured in five locations per individual micrograph in the OJZ and comparison areas. Images of the OJZ were analyzed if an ELMd was present, either in the same image or as part of a multi-image montage. In the comparison area, retinal detachment was clean (i.e., no OS tips adhered to either apical RPE or subretinal material). Thus IPS was measured to the tips of the OS. The detached retina and RPE-BrM complex were assessed separately for thickness and volume occupancy, and results were combined. Differences between measurable tissue component volumes in the OJZ and comparison areas were evaluated for statistical significance using two-sided *t*-tests (StatPlus for Mac, v. 8, AnalystSoft), without correction for multiple comparisons. Two-sided tests were used because tissue elements in the OJZ might be either higher (BLamD) or lower (OS) than in the comparison area. Features occupying <1% in the OJZ (Sloughed RPE, Shed Aggregates) were not analyzed further. A P value <0.05 was considered significant.

Results

Automated Determination of Photoreceptor and RPE Degeneration in OCT

Figure 1 and Supplementary Figure S3, respectively, show B-scans representative of the OCT volumes acquired at the last clinic visit and used for determining the area of atrophy in the index (left) and fellow (right) eyes. Areas of RPE loss and rPSi are shown on the B-scans as blue and green overlays, respectively. Of importance for contextualizing the ultrastructural results below is the appearance at baseline of rPSi superonasal to the fovea in Figure 1. This area expands and eventually includes RPE degeneration over the five-year observation period.

Figure 2 and Supplementary Figure S4, respectively, are axially expanded OCT scans through the fovea of the index eye and fellow eyes. These demonstrate fine details in the high-quality scans ($Q > 35$) submitted for automated analysis

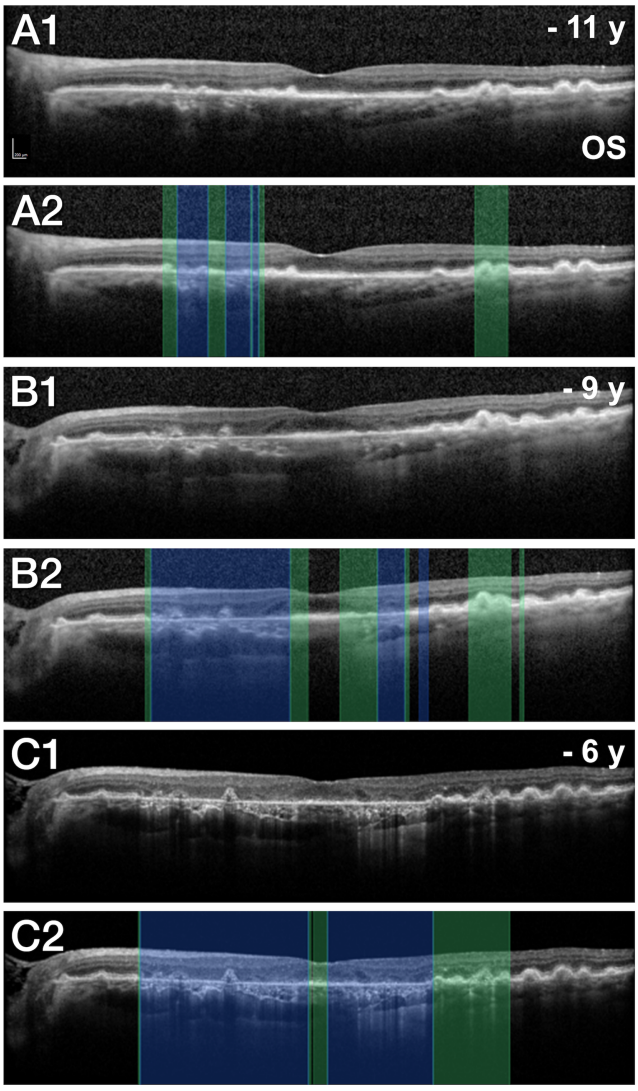

Figure 1. Regions in OS with photoreceptor degeneration and RPE loss detected in OCT: Representative OCT B-scans of the index eye (OS) over five years are shown. Scans with and without an overlay from automated OCT segmentation[21,25,26] display reduced photoreceptor segment visibility (rPSi, *green*) and RPE loss (*blue*) within a 6 × 6 mm square. See Methods for details. **(A)** In a central OCT scan, typical AMD-associated changes are observed, including drusen, hyperreflective foci, and alterations of the RPE and photoreceptors (**A1**). rPSi (*green*) and RPE loss (*blue*) without foveal involvement are shown, 11 years before death. Over time, existing drusen may remain stable, progress, or regress, resulting in new areas of rPSi and RPE loss **(A1–C1)**. RPE loss is typically preceded by rPSi. Details of features visible at the last time point are available in Figure 2. *Bar* **A1**: 200 µm.

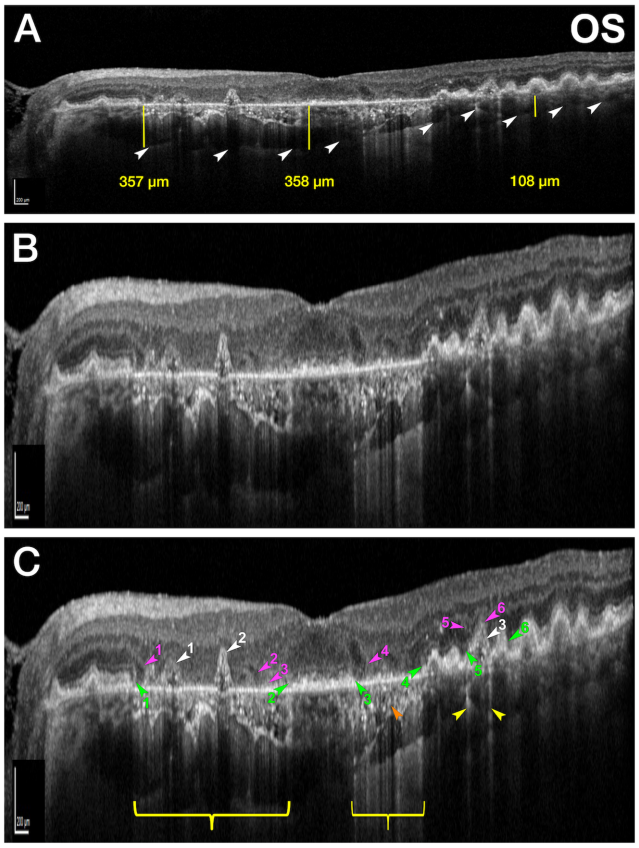

Figure 2. Annotated OCT shows atrophy details in OS, six years pre-mortem: **(A)** OCT B-scan through the fovea of the index eye at the last clinic visit (ART 9, Quality 36). *White arrowheads* indicate the choroid-sclera junction. The nasal choroid has enlarged vessels and is thicker than temporal choroid. Indicated thicknesses were measured at the vertical lines. **(B)** Scan of panel **A** is expanded axially. **(C)** In the expanded scan of panel *B*, *green arrowheads* in pairs mark descents of the ELM that bound areas of atrophy (between green arrowheads 1–2, 3–4, and 5-6). *Pink arrowheads* indicate OPL subsidence. *Pink arrowhead 4* marks a Monés wedge. *Pink arrowheads* 2–3 may represent an atypical wedge with less pronounced OPL subsidence. *White arrowheads* indicate calcified drusen lacking both RPE and obvious coverings of persistent basal laminar deposit ("tombstone deposits"). Prominent hypertransmission is visible beneath atrophic regions (*yellow brackets*). *Yellow arrowheads* indicate pinstripe hypertransmission surrounding deposits.[51] The *orange arrowhead* highlights punctate hyperreflectivity within the choroid, attributed to cells (melanocytes, mast cells, macrophages).

and the symmetry of pathology in the two eyes. Both figures show ELMd bounding large and small patches of atrophy, wide hypertransmission into the choroid in atrophy meeting cRORA criteria, narrow hypertransmission at the perimeters of deposits,[51] OPL subsidence, and calcified drusen without overlying RPE or obvious BLamD ("tombstone deposits"). The latter can be compared to a druse capped by RPE in Supplementary Figure S4. In both eyes, the inner choroid contains punctate hyperreflectivity indicating cells.[52] Overall choroid thickness is greater nasally than temporally because of enlarged vessels of the outer choroid.

Figure 3 and Supplementary Figure S5 map RPE loss (blue) and rPSi (green) in the index and fellow eyes, respectively. In both eyes at baseline, the area of rPSi covers the ETDRS inner ring, and it spares the fovea. The border is irregular, as expected given the origin of atrophy over individual drusen. Over five years, this area expands into the fovea and fills in irregularities to create a continuous area of PR degeneration. The superimposed overlays show that rPSi exceeds RPE loss, thus preceding it in appearance on OCT. RPE loss expands disproportionately to nearly approximate that of the rPSi. In both eyes, the fovea was overtaken between six and nine years before death.

Figure 4 and Supplementary Figure S6 graphically depicts atrophy expansion in the photoreceptor segments and RPE-BrM bands as computed from the OCT volumes of the index

Investigative Ophthalmology & Visual Science

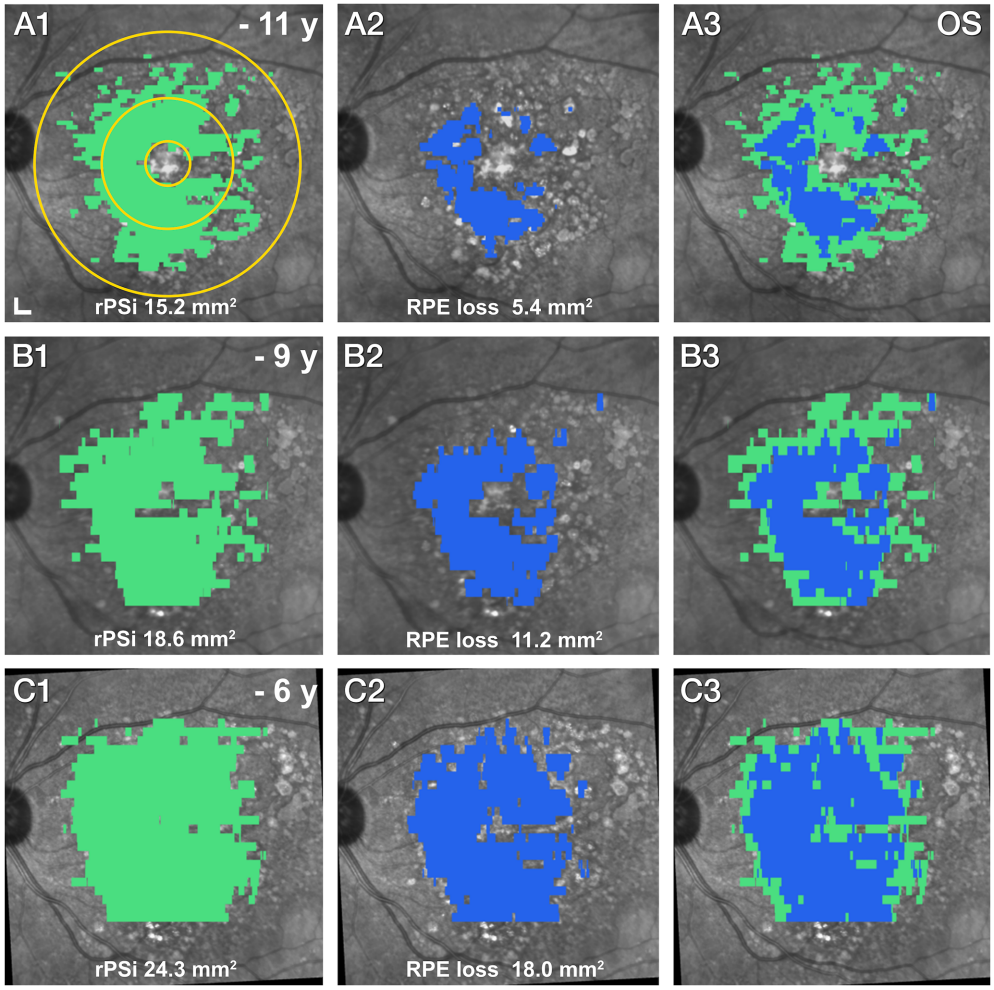

Figure 3. Progression of photoreceptor degeneration and RPE loss in OCT volumes. Areas of rPSi and RPE loss are green and blue overlays, respectively, on en face near infrared reflectance images over five years. These were mapped within a 6 × 6 mm square. An ETDRS grid is shown for reference. See Methods for details. *Scale bar*: 500 µm **(B1)**. **(A1–C1)** rPSi spares the fovea and fills to the middle of ETDRS inner ring with irregular borders at baseline. Both the fovea and the borders fill in by six years. **(A2–C2)** RPE loss is smaller and spares the fovea at all time points. **(A3–C3)** Superimposition of the two overlays shows that rPSi precedes RPE loss, and the RPE loss expands disproportionately.

and fellow eyes, respectively. In the A panels of both figures, RPE loss starts smaller and expands faster than rPSi, as shown by the slightly steeper slope for RPE, and as expected from the maps. Panels B and C of both figures show that the overall area of RPE loss expands more rapidly than rPSi. Calculated growth rates for the left eye are 2.432 and 1.770 mm^2/yr for RPE and rPSi, respectively. Expressed as equivalent radius, rates are 0.368 and 0.200 mm/yr, respectively. Areas of rPSi and RPE loss in the fellow eye expanded at a slightly slower rate than in the index eye; the overall pattern was similar.

Outer Junctional Zone Versus Temporal Area, Qualitative and Quantitative Comparison

B-scans and supporting histology in the OJZ superior and nasal to the main atrophy area, and in the temporal comparison area are shown in Figure 5. At a superior level (Figs. 5A1, 5A2), the OJZ has numerous OS despite the presence of a continuous layer of SDD. At the level of the optic nerve head (Figs. 5C1, 5C2), the OJZ has a clear ELMd, photoreceptors are shortened and reduced in number, and the RPE is dysmorphic but continuous. In the comparison area (Figs. 5B1, 5B2), OS are relatively abundant. A thin layer of subretinal material overlies the RPE but is not attached to the photoreceptors. Inferior and temporal to the atrophic area, there are large calcified drusen (Figs. 5D1, 5D2), over which photoreceptors are shortened or absent. The RPE is thin yet continuous, atop a thick BLamD. We did not see lightly pigmented cells suggestive of phagocytes between RPE and photoreceptors.[53]

Figure 6 shows a representative TEM image of the comparison area. The inner segments are full length, with visible myoid and ellipsoid portions. Ellipsoids contain long tightly packed mitochondria. OS appear full length and surrounded by space; the interphotoreceptor matrix, a delicate extracellular matrix, was not detected in our specimen. We observed material consistent with the dimensions and location of SDD atop the RPE but lacking the typical internal ultrastructure.[54,55] The average estimated distance between the ELM and the RPE basal lamina was 87.6 ± 6.9 µm (Table).

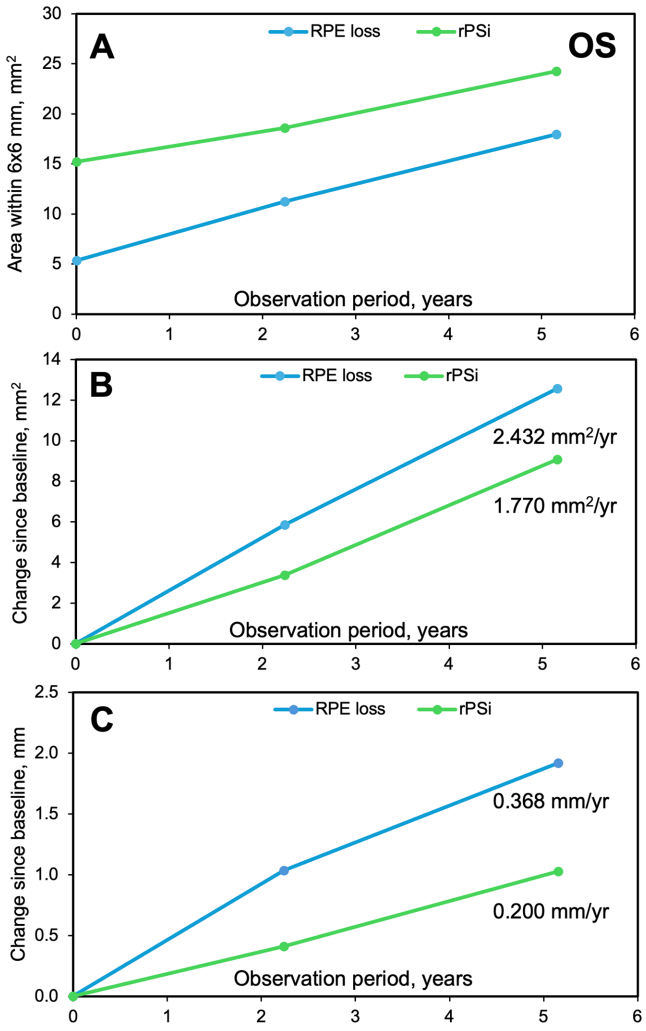

Figure 4. Growth of atrophy in index eye determined from OCT volumes. Areas of RPE loss and rPSi were determined by automated analysis of OCT volumes acquired at 11, nine, and six years before death. Measurements were taken within a 6 × 6 mm area. The first time point serves as the baseline, although RPE atrophy was already present. Yearly rates of expansion on the graphs were determined by linear fits to data at these three time points. **(A)** Area of RPE loss and rPSi within a 6 × 6 mm square. RPE loss area starts smaller and expands faster than rPSi, as shown by the slightly steeper slope. **(B)** Yearly growth rate in area (mm^2). **(C)** Yearly growth rate expressed as an equivalent radius (in mm).

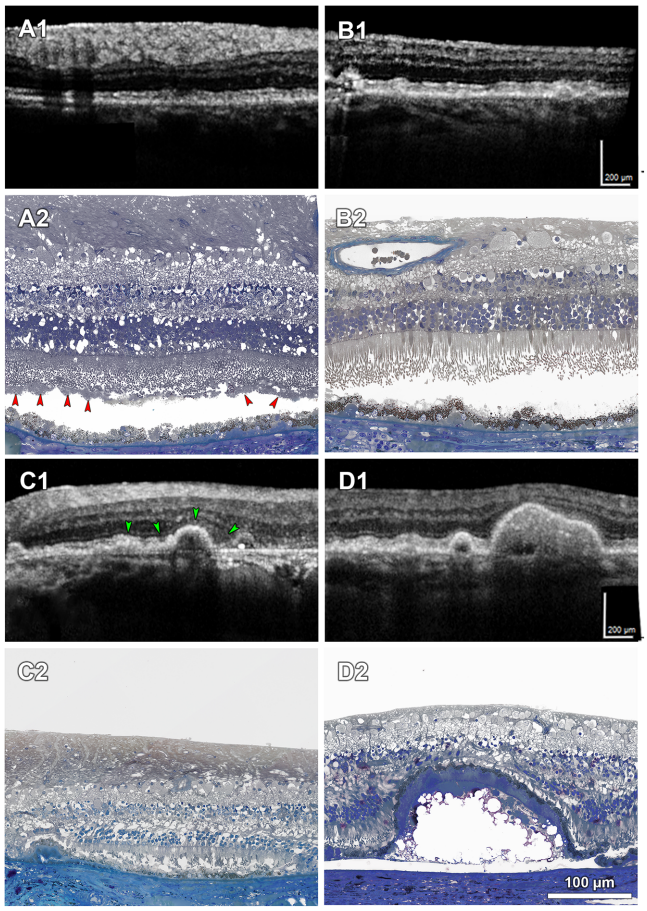

Figure 5. OCT-histology comparisons in geographic atrophy. **(A1, B1, C1, D1)** B-scans were captured at the last clinic visit, six years before death, and are representative of areas included in the automated quantification of atrophy (see Figure 3). Quality is 36 for A1–B1 (scan 29) and 42 for C1–D1 (scan 16). Automated real-time averaging is 10. **A2, B2. C2, D2.** High-resolution histology representative of areas shown by OCT, magnified 5.6-fold (compare scale bar in D2 to B1, D1). Detachments of neurosensory retina from RPE were approximated digitally. **(A1, A2, C1, C2)** Outer junctional zone superior nasal to the main atrophic area. SDD (*red arrowheads*) was split such that part remained attached to the tips of the photoreceptors, giving the impression of a "lifted veil." **(B1, B2)** Relatively uninvolved retina temporal to the main atrophic area is representative of the comparison areas used for tissue component quantification. Outer segments are relatively abundant. A thin layer of subretinal material overlies the RPE but is not attached to photoreceptors. **(D1, D2)** Photoreceptors are shortened or missing atop a large druse (d) filled with calcific nodules, most of which were dislodged. The RPE is thin yet continuous atop a thick BLamD. The retina was detached from most other drusen in this region.

Figure 7 shows a representative area of OJZ and ELM descent nasal to the main atrophic area. The RPE is highly misshapen but continuous. A few OS remain, and the interphotoreceptor space around them is greatly diminished. Inner segments are stunted and filled with globular mitochondria. A myoid portion is barely detectable. At the ELM descent, within stubby cone inner segments, fragmented mitochondria translocate inwardly, across the ELM descent, toward the cell body in the outer nuclear layer (ONL). Again, no cells consistent with phagocytes were seen. The mean distance between ELM and RPE basal lamina in the OJZ is 43.9 ± 5.8 µm (Table), a reduction of 50%.

Quantitative results for the OJZ and comparison area are based on running lengths of 4160 µm vs 4415 µm, a total of 2103 and 3675 scored points, in 20 and 22 images, respectively (Table). The percentage of ineligible points was 2.5% for the OJZ and 0.4% for the comparison area. Most evaluated areas were near the OCT levels shown in Figure 1. Figure 8 shows that photoreceptor-related components in the OJZ are significantly lower ($P < 0.05$) than in the comparison area and notably specific to different sections of the cells. Relative to the comparison area, OS and IPS volumes are both reduced to 16%, ISmy is reduced to 25% (as ellipsoids with fissioning mitochondria telescope into the myoids), and ISel are reduced to 45%. Results for non-photoreceptor components differed. Despite clearcut RPE dysmorphia in the OJZ, RPE volume in the OJZ was similar to the Comparison area (104%). BLamD

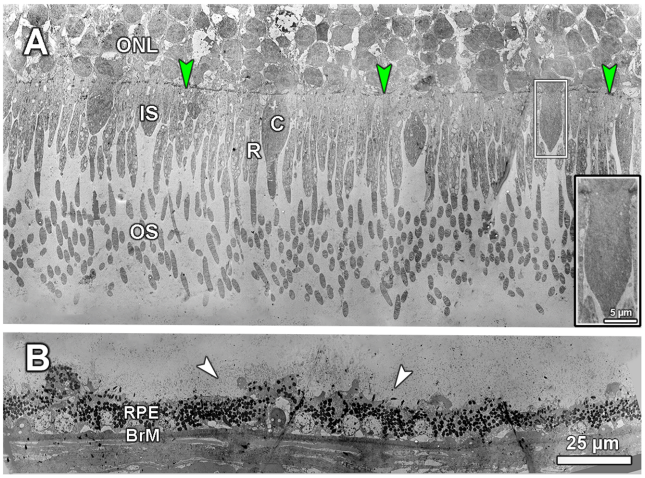

Figure 6. Ultrastructure of comparison area temporal to atrophy. **(A)** Outer segments and surrounding interphotoreceptor space are abundant. **(B)** Subretinal material (*white arrowheads*) was consistent with location and abundance of SDD but lacked expected ultrastructure[55] due to suboptimal preservation. Images of retina detached from RPE in **A** and **B** were digitally approximated from separate sections. C, cone; R, rod.

Table. Sample Size and Layer Thicknesses

	OJZ	Temporal
Number of images	20	22
Sample length, µm	4160	4415
Total scored points	2103	3675
Ineligible points	2.5%	0.4%
ELM–RPEBL, µm, mean	43.9	87.6
ELM–RPEBL, µm, SD	5.8	6.9
ELM–RPEBL, CV	13%	8%

CV, coefficient of variation; ELM–RPEBL, distance between ELM and RPE basal lamina.

Points overlying unrecognizable tissue components or preservation/processing artifact were ineligible for scoring.

was present in the OJZ and either absent or underrepresented in the comparison area. An AMD hallmark is BLamD abundance in the central area[56–58] that may also be found at lower frequency peripherally.[59–61]

Visibility of Mitochondria Fission and Translocation at the ELM Descent

Fragmented mitochondria like those at the ELMd of the OJZ were also seen in cones over a calcifying druse (Supplementary Fig. S7). Fragmented mitochondria in AMD were first photo-documented for ORT, a scrolling of photoreceptors by Müller glia that creates protrusions of the subretinal space, continuous with the border of atrophy.[28,29] Within the photoreceptors, this process was considered mitochondrial fission, resulting in a myriad of reflective surfaces at the characteristic border of ORT. We thus hypothesized that in some locations of the index eye the ELMd may be thickened laterally and especially reflective. Examples of both thickened and typical ELMd in B-scans from the index and fellow eye are shown in Figures 9A and 9B. Thickened ELMd is very striking in images of other eyes with GA that are acquired with <3 µm axial resolution OCT (Fig. 9C).

Discussion

Automated analysis of high-quality OCT volumes show that rPSi area exceeded RPE loss area in both eyes of this case of bilateral GA in AMD. Although RPE loss initially involved a smaller area, it expanded more rapidly than rPSi, leading to convergence of the two regions over time. Complementary, computer-assisted analysis of TEM images indicates that photoreceptor degeneration is severe and sectionally specific, whereas RPE remains continuous albeit dysmorphic. Notably, we provide the first quantitative histologic assessment of photoreceptor loss in this context, revealing an 85% reduction of outer segment mass in the OJZ, accompanied by marked reduction of the surrounding extracellular space.

This bilateral GA case, of which OS is featured here, illustrates both typical and atypical aspects of the disease.[17] GA is frequently bilateral, with half of patients developing GA in both eyes within seven years of initial GA diagnosis.[62] GA lesion morphology is often similar in the two eyes,[63,64] as seen in ours. Regarding lesion multifocality, AREDS2 trial data indicated a multifocal GA configuration at first appearance in 24.6% of eyes with GA (of 1616).[65] Regarding foveal involvement over time, 67.0% of eyes in the AREDS2 dataset exhibited non-central GA at first appearance,[65] and 62.6% of eyes ($N = 147$) in a population-based natural history study pooling four European and Australian cohorts lacked initial central foveal involvement,[66] consistent with foveal sparing early in the disease course. These percentages, which depend on study design, imaging protocols, stage of disease, and lesion definitions, are provided for context and are not intended to imply generalizability or prevalence estimates from our single-eye clinicopathologic study.[17] An unusual aspect of both eyes, seen by OCT, was notable venous congestion within a thick choroid, common in Asian populations[67,68] and less common but possible in persons of European descent.[69,70]

We used the term "rPSi" for a composite OCT measure that includes photoreceptor ellipsoids and OS, two distinct sections of these cells. rPSi corresponds to similar measures with different names used by other research groups.[19,22,31,71,72] rPSi includes both reduction of a distance and non-visibility of cells, two mechanistically distinct phenomena that cannot be separated with the resolution of imaging devices used in this patient's care. Reduced distance means shortening of photoreceptor segments and likely also shortening of the melanosome-bearing RPE apical processes. These surround the outer two-thirds of the OS[33,73] and contribute to the interdigitation zone. Non-visibility means that photoreceptor integrity cannot be measured either because cells died or because they are hyporeflective due to deflection or other perturbation that degrades waveguiding. A clear example of invisible yet still-living photoreceptors is the hyporeflective annulus of stage 3 SDD signifying an EZ break in magnified spectral domain OCT, and by histology, individual deposits poking into a forest of photoreceptor segments.[6,7,74] A direct comparison of rPSI with other measures is beyond the scope of the current report and a focus of ongoing nomenclature harmonization by the International Retinal Imaging Society and other organizations.

We kept the term "RPE loss" as the area of deep hypoautofluorescence on which the OCT metric was trained, corresponding to an area devoid of a continuous RPE layer. Our measured yearly linear growth rate of 0.368 mm/yr is higher

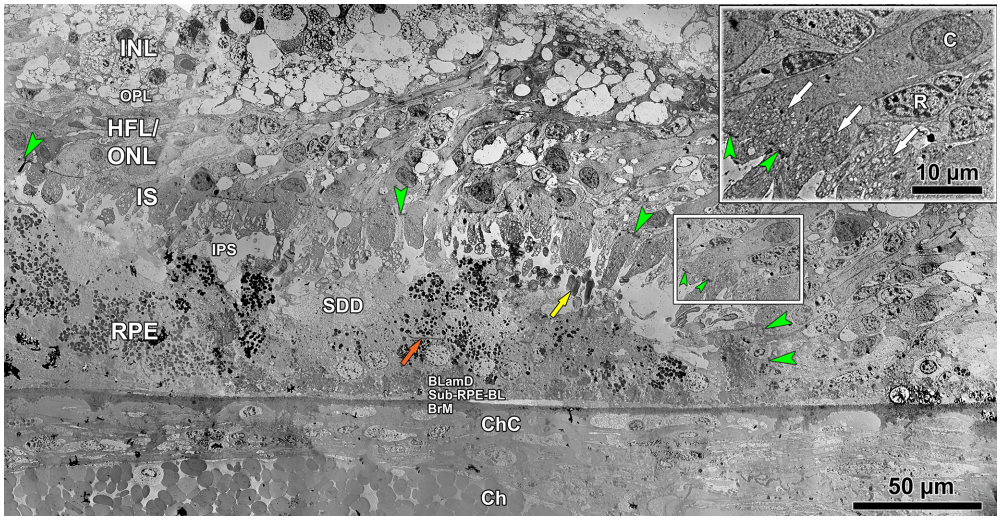

Figure 7. Ultrastructure of outer junctional zone, nasal to the main atrophic area. **(Main panel)** The ELM descent (*green*) is the border of atrophy in the neurosensory retina. RPE is highly misshapen but continuous, with a visible actin cytoskeleton belt (*orange arrowhead*). Some outer segments (*yellow arrow*) remain with IPS around them. IPS normally contains interphotoreceptor matrix, which was not detected. Some SDD is visible. IS are short and filled with fragmented but recognizable mitochondria. Thinner IS representing rod photoreceptors are few in number. **(Inset)** Cone IS at the ELM descent (*green arrowheads*) contain fragmented mitochondria (i.e., undergoing fission), translocating inwardly toward cone cell bodies in the outer nuclear layer (C, cone nucleus, R, rod nucleus).

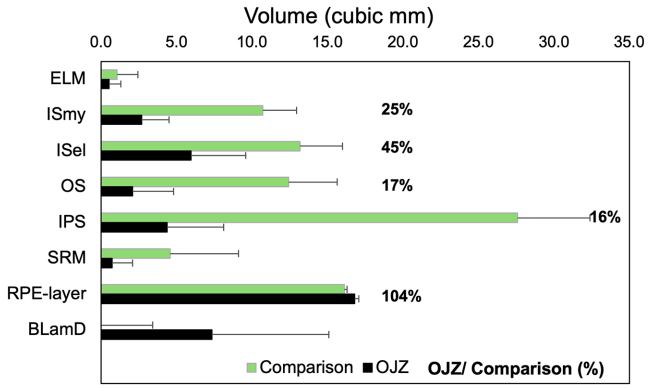

Figure 8. Quantification of tissue components in outer junctional zone and comparison area. Volume of outer retinal tissue components in the OJZ nasal to atrophy is compared to a less affected comparison area temporal to atrophy and expressed as OJZ/comparison (%). Volume occupancy (%) was determined from transmission electron micrographs taken from the two areas (sample size in Table). Occupancies were converted to volumes (mm^3) in a 1 mm unit square using the mean distance between the ELM and the outer boundary of BLamD as the third dimension. All differences between OJZ vs. Comparison were significant at $P < 0.05$ except ELM and RPE in two-sided t-tests. Only tissue components (see Methods) that were found in the OJZ are shown.

than the average 0.199 ± 0.012 mm reported for multifocal GA in a metanalysis of many CFP images.[75] It is also higher than our previous estimate for this case of 0.198 mm/ year applying custom image analysis to fundus autofluorescence images (λ_{ex} = 532 nm, Supplementary Fig. S1). Bilateral GA tends to expand faster than unilateral.[65,76] Atrophy growth in our case was both continuous with and separate from existing areas of atrophy,[77] as evidenced by the ragged border in the maps. The faster rate of RPE progression does not contradict the greater area of rPSi than RPE loss at baseline. We consider rPSi to start earlier on a wider scale than RPE loss, with the area of RPE loss approaching that of rPSi, over time. This can happen only if the area of RPE loss expands faster than rPSi during the observation window (Fig. 4). Relative to RPE loss, the earlier onset, wider extent, and differential treatment response of rPSi in trials suggests that fundamentally different mechanisms underlie degeneration in these two cell populations.

The maps of Figure 3 and Supplementary Figure S5 show that atrophy expands at single spots along the RPE loss border. Per analysis of color photographs,[75] multifocal atrophy starts atop individual drusen and grows faster than unifocal lesions, in proportion to the total perimeter. A histologic basis for drusen-driven atrophy is available from our prior studies[2,78–80] that included analysis of 45 unique drusen from the current index eye.[17] In brief, as photoreceptors degenerate and shorten over drusen, the ELM approaches the druse apex where the RPE remains continuous. Where photoreceptors have died, the ELM, made exclusively of Müller glia by that time, encircles a gap in the RPE layer. The RPE cannot seal this gap, we suspect, because Müller glia prevent it from doing so, thus initiating atrophy. Such a lifecycle is plausible for drusen that progress to atrophy. However, we do not know and cannot determine from the current study which drusen might have resolved without atrophy and with reappearance of outer retinal bands.[11]

We found that photoreceptor degeneration in the OJZ is disproportionately and sectionally specific, with OS and the surrounding interphotoreceptor space being most severely affected, followed by ISmy. This difference likely represents true loss, not only displacement of photoreceptor components by pathologic material, because we measured volumes (mm^3) of all components between the ELM and the RPE-BL visualized comprehensively with TEM. Photoreceptors are divided vertically into functionally and ultrastructurally distinct sections that are horizontally aligned, creating the outer retinal bands of OCT.[54] Individual photoreceptors undergo significant subcellular reorganization in advanced AMD, as captured in part by prior histological studies of

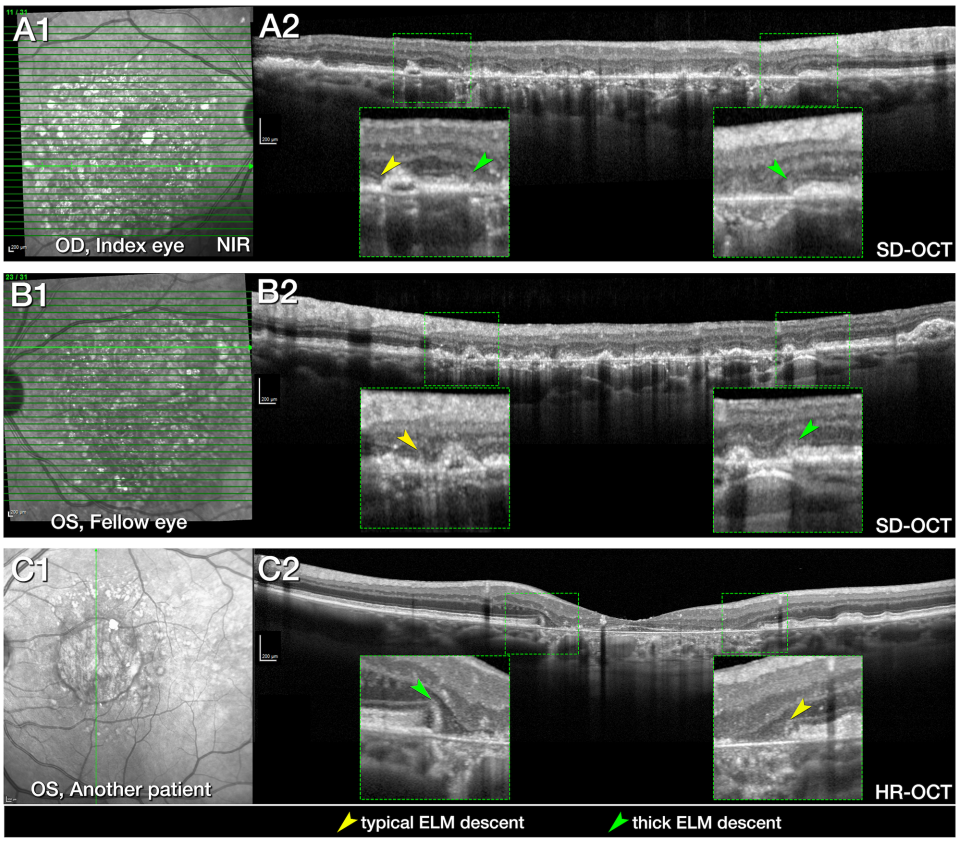

Figure 9. Thickened ELM descent, a possible biomarker for mitochondrial fission. **A1** and **B1** show near-infrared reflectance (NIR) images from the index (left) and fellow (right) eye of the current report, obtained at the last clinical visit, six years before death. **A2** and **B2** depict horizontal B-scans demonstrating typical and less typical AMD findings. Two morphologies of ELMd are visible in magnified insets: a typical thin ELMd (*yellow arrowheads*) and a thickened and hyperreflective ELMd (*green arrowheads*). **C1** and **C2** show images from a second patient, with a large foveal involving GA lesion and a vertical HR-OCT scan (<3 µm axial resolution) through the center. HR-OCT reveals both a typical thin ELMd (*yellow arrowhead* right magnified insets, **C2**) and a thickened and hyperreflective ELMd (green arrowhead, left magnified insets, **C2**). *Scale bars* in **A2-B2-C2**: 200 µm.

GA. These include inwardly retracted photoreceptor nuclei and an absence of ONL in the inner junctional zone,[40] overall shortening of the myoid,[81] apoptotic photoreceptor nuclei,[82] scattered cone cell bodies inside an atrophic area lacking a continuous RPE layer, and degenerating photoreceptors outside this area.[45] Photoreceptors degenerate from the outer segments inward, in OCT of GA[83] and retinitis pigmentosa,[84] as they do in many animal models.[85] Thus outer segment degeneration in GA is visible further out in OCT than degeneration of either inner segments or ONL.[83]

We estimated for the first time IPS volume in an AMD eye and found it reduced by ~85%. Because the interphotoreceptor matrix itself was not visible in our specimens, we measured space between grouped OS, whose uniform length suggested that they were not broken by the detachment. Recently, interphotoreceptor matrix in a young adult human retina[33] was quantified for the first time and found to occupy 38% of the space between the ELM and the inner surface of the RPE cell bodies. Noninvasive imaging measures of photoreceptor energy utilization in animal models affirm a dynamic regulation of this space by light in relation to tissue hydration. In the dark, the distance between the ELM and RPE shrinks,[86–88] and interphotoreceptor matrix proteins redistribute.[89,90] Our estimates of drastically reduced IPS draw attention to an underappreciated aspect of advanced AMD. A shrunken distance from ELM to RPE-BL visible in OCT indicates acidification of the space around photoreceptors. Further, it represents reduced availability of key molecules such as interphotoreceptor retinoid binding protein, a pro-survival and antioxidant chaperone.[91,92] Thus a hostile environment for photoreceptors may be made worse.

We observed thickened ELMd, a feature seen on high-resolution OCT (Fig. 9), adaptive optics–assisted OCT,[93] and in numerous published examples of spectral-domain OCT[94–102] This interpretation is supported by our prior investigations of the reflective border of ORT in advanced AMD. These in turn rest on seminal biophysics research demonstrating that mitochondria and lysosomes are highly reflective (via Mie scattering).[103–105] Our ORT studies included direct clinicopathologic correlation, histochemistry, high-resolution light microscopy, TEM, and three case series, one longitudinal and including outer retinal atrophies, as well as AMD.[28,29,81,106-108] Collectively this prior research established that ORT consisted almost exclusively of cones, the ORT reflective border corresponded to inner segments containing fragmented mitochondria in transit towards photoreceptor somata, and that the ELM border of ORT was continuous with the ELM border of atrophy. These imaging features have been since replicated and extended by others.[109]

Whether histologically fragmented cone mitochondria over drusen and within the OJZ are reliably detectable on OCT (Fig. 9), remains uncertain. It is also unclear whether such OCT features directly correspond to molecularly defined mitochondrial fission. Mitochondria including those in cone ISel respond to energy needs, environmental stimuli, and ongoing quality control by fusion and fission to form larger and smaller organelles, respectively.[110,111] Fission facilitates sequestration of irreparably damaged components for bulk elimination by mitophagy, involving transport toward the soma.[110] Although mitochondria represent an emerging therapeutic target in AMD,[112,113] the photoreceptors with fragmented organelles observed here likely represent an advanced—and possibly irreversible—stage of degeneration.

Limitations of our study are acknowledged. Only three OCT volumes were analyzed for growth rate, yet these had the most B-scans of those available, and they fortuitously spanned the five-year observation period. Cropping OCT volumes to 6 × 6 mm may have biased downward the estimated expansion in rPSi. Our lesions exceeded 10 mm^2, a threshold beyond which lesions measured in OCT are slightly larger than those measured by fundus autofluorescence although still highly correlated.[24] Our data cannot be considered a direct validation of segmentation due to a 6-year gap between last clinic visit and death and TEM analysis limited by tissue- and section-level artifacts. We did not examine other aspects of photoreceptor degeneration such as thinning[83] or ONL dyslamination,[40] and we did not address other potentially meritorious photoreceptor metrics like ONL thickness.[114] Our data do not explain the clinical trial results used for algorithm training or the mechanism of action of the trialed drugs. Our data cannot address the chicken-or-egg question of which layer degenerates first in AMD, because we did not assess all relevant layers. Indeed, a strong candidate for the differential mechanisms mentioned above is widespread choriocapillaris dysfunction in GA[115–119] that starts under the central retina in aging,[120–124] and jeopardizes the distant photoreceptors more than the adjacent RPE. Our study was exploratory, with both hypothesis- generating and -testing aspects. This is one case, and results should be generalized cautiously.

Strengths of this report include one GA case with excellent clinical imaging over five years, an atrophy growth rate calculated from OCT volumes using state-of-the-art and previously validated automated methods, and comprehensive tissue visualization by TEM and quantification with new tools. In conclusion, we presented the first clinicopathologic correlation of an eye with GA secondary to AMD and a known atrophy growth rate. In this one eye with GA, both OCT and microscopically assessed photoreceptor degeneration is more severe than RPE degeneration. We present hypothesis-generating data suggesting that numerous tiny mitochondria undergoing inward translocation within cones may represent fission, an irreversible step in cell death, and a hyperreflective OCT biomarker. Determining the best OCT metrics and acceptable nomenclature for photoreceptor degeneration in AMD is an ongoing initiative, for which this report may be helpful.

Acknowledgments

The authors thank Yonejung Yoon, MSc, PhD, of The Eye-Bank for Sight Restoration (NYC) for timely retrieval of donor eyes, and Melissa Chimento at the High-Resolution Imaging Facility at UAB for guidance on use of the electron microscope.

Supported by The Macula Foundation, Inc., New York, NY; unrestricted funds to the Department of Ophthalmology and Visual Sciences (UAB) from Research to Prevent Blindness, Inc., and EyeSight Foundation of Alabama. AB reports grants from the Dr. Werner Jackstädt-foundation. The Carl G. and Pauline Buck Trust funded the slide scanner. Sponsors had no role in the design and conduct of the study; collection, management, analysis, and interpretation of the data; preparation, review, or approval of the manuscript; and decision to submit the manuscript for publication. Fundamental research in OCT validation (CAC, JDM) and Müller glia biology (MME) was supported by NIH grants R01EY06109 and NIH R01 EY031044, respectively.

Portions of this research have been presented at the Association for Research for Vision and Ophthalmology 2025 annual meeting (Salt Lake City UT USA).

Contribution Statements: All authors helped draft the article or revise it critically for important intellectual content. All authors approved the final version. Drs. Bijon and Freund had full access to all clinical data. Drs. Curcio and Messinger had full access to all laboratory data. Dr. Berlin liaised with RetinSight. Drs. Leingang and Huemer analyzed de-identified OCT volumes. These authors are responsible for data integrity and accuracy. Dr. Sloan wrote the FIJI plug-in for guided point-counting. Study conception and design: CAC, AB, KBF, MME; all authors. Acquisition of data: AB, CAC, JDM, OL. Analysis and interpretation of data: All authors. Writing of manuscript: CC; all authors.

Disclosure: **C.A. Curcio**, Heidelberg Engineering (R), Genentech/Hoffman LaRoche (C), Apellis (C), Astellas (C), Boehringer Ingelheim (C), Character Biosciences (C), Osanni (C), Annexon (C), Mobius (C), Ripple (C), Octant (C), Merck (C), Sanofi (C), SparingVision (C), Ikarovec (C); **J.D. Messinger**, None; **K.R. Sloan**, None; **M.M. Edwards**, None; **J. Bijon**, None; **F. Huemer**, None; **O. Leingang**, None; **K.B. Freund**, AstraZeneca (C), Apellis Pharmaceuticals (C), EyePoint Pharmaceuticals (C), Genentech (C), Novartis Pharma AG (C), Regeneron Pharmaceuticals, Inc. (C); **A. Berlin**, None

References

1. Sadda SR, Guymer R, Holz FG, et al. Consensus definition for atrophy associated with age-related macular degeneration on optical coherence tomography: CAM Report 3. *Ophthalmology*. 2018;125:537–548.
2. Guymer RH, Rosenfeld PJ, Curcio CA, et al. Incomplete retinal pigment epithelial and outer retinal atrophy (iRORA) in age-related macular degeneration: CAM Report 4. *Ophthalmology*. 2020;127:394–409.
3. Jaffe GJ, Chakravarthy U, Freund KB, et al. Imaging features associated with progression to geographic atrophy in age-related macular degeneration: CAM Report 5. *Ophthalmol Retina*. 2021;5:855–867.
4. Heier JS, Lad EM, Holz FG, et al. Pegcetacoplan for the treatment of geographic atrophy secondary to age-related macular degeneration (OAKS and DERBY): two multicentre, randomised, double-masked, sham-controlled, phase 3 trials. *Lancet*. 2023;402:1434–1448.
5. Khanani AM, Patel SS, Staurenghi G, et al. Efficacy and safety of avacincaptad pegol in patients with geographic atrophy (GATHER2): 12-month results from a randomised, double-masked, phase 3 trial. *Lancet*. 2023;402:1449–1458.
6. Curcio CA, Messinger JD, Sloan KR, McGwin G, Jr, Medeiros NE, Spaide RF. Subretinal drusenoid deposits in non-neovascular age-related macular degeneration:

morphology, prevalence, topography, and biogenesis model. *Retina*. 2013;33:265–276.
7. Zhang Y, Wang X, Blanco E, et al. Photoreceptor perturbation around subretinal drusenoid deposits revealed by adaptive optics scanning laser ophthalmoscopy. *Am J Ophthalmol*. 2014;158:584–596.
8. Miller DT, Kurokawa K. Cellular-scale imaging of transparent retinal structures and processes using adaptive optics optical coherence tomography. *Annu Rev Vis Sci*. 2020;6:115–148.
9. Wang Q, Tuten WS, Lujan BJ, et al. Adaptive optics microperimetry and OCT images show preserved function and recovery of cone visibility in macular telangiectasia type 2 retinal lesions. *Invest Ophthalmol Vis Sci*. 2015;56:778–786.
10. Goerdt L, Raming K, Rodriguez Garcia JL, Pfau K, Holz FG, Herrmann P. Ellipsoid zone recovery in macular telangiectasia type 2. *Retina*. 2024;44:1413–1421.
11. Mones J, Pagani F, Santmaria JF, et al. Spontaneous soft drusen regression without atrophy and the drusen ooze. *Ophthalmol Retina*. 2025;9:828–837.
12. Chew EY, Gillies M, Jaffe GJ, et al. Cell-based ciliary neurotrophic factor therapy for macular telangiectasia type 2. *NEJM Evid*. 2025;4:EVIDoa2400481.
13. Pfau M, von der Emde L, Dysli C, et al. Light sensitivity within areas of geographic atrophy secondary to age-related macular degeneration. *Invest Ophthalmol Vis Sci*. 2019;60:3992–4001.
14. Zanzottera EC, Ach T, Huisingh C, Messinger JD, Freund KB, Curcio CA. Visualizing retinal pigment epithelium phenotypes in the transition to atrophy in neovascular age-related macular degeneration. *Retina*. 2016;36(1):S26–S39.
15. Zanzottera EC, Ach T, Huisingh C, Messinger JD, Spaide RF, Curcio CA. Visualizing retinal pigment epithelium phenotypes in the transition to geographic atrophy in age-related macular degeneration. *Retina*. 2016;36(1):S12–S25.
16. Dolz-Marco R, Balaratnasingam C, Messinger JD, et al. The border of macular atrophy in age-related macular degeneration: a clinicopathologic correlation. *Am J Ophthalmol*. 2018;193:166–177.
17. Curcio CA, Messinger JD, Berlin A, et al. Fundus autofluorescence variation in geographic atrophy of age-related macular degeneration, a clinicopathologic correlation. *Invest Ophthalmol Visual Sci*. 2025;66:49.
18. Riedl S, Vogl WD, Mai J, et al. The effect of pegcetacoplan treatment on photoreceptor maintenance in geographic atrophy monitored by artificial intelligence-based OCT analysis. *Ophthalmol Retina*. 2022;6:1009–1018.
19. Schmidt-Erfurth U, Mai J, Reiter GS, et al. Disease activity and therapeutic response to pegcetacoplan for geographic atrophy identified by deep learning-based analysis of OCT. *Ophthalmology*. 2024;132:181–193.
20. Mai J, Lachinov D, Reiter GS, et al. Deep learning-based prediction of individual geographic atrophy progression from a single baseline OCT. *Ophthalmol Sci*. 2024;4:100466.
21. Lachinov D, Seeböck P, Mai J, Goldbach F, Schmidt-Erfurth U, Bogunovic H. Projective skip-connections for segmentation along a subset of dimensions in retinal OCT. *International Conference on Medical Image Computing and Computer-Assisted Intervention 2021 Sep 21*. Cham: Springer-Verlag; 2021:431–441.
22. Vogl WD, Riedl S, Mai J, et al. Predicting topographic disease progression and treatment response of pegcetacoplan in geographic atrophy quantified by deep learning. *Ophthalmol Retina*. 2022;7:4–13.
23. Mai J, Reiter GS, Riedl S, et al. Quantitative comparison of automated OCT and conventional FAF-based geographic atrophy measurements in the phase 3 OAKS/DERBY trials. *Sci Rep*. 2024;14:20531.
24. Mai J, Riedl S, Reiter GS, et al. Comparison of FAF versus OCT-based evaluation of the therapeutic response to pegcetacoplan in Geographic Atrophy. *Am J Ophthalmol*. 2022;244:175–182.
25. Orlando JI, Gerendas BS, Riedl S, et al. Automated quantification of photoreceptor alteration in macular disease using optical coherence tomography and deep learning. *Sci Rep*. 2020;10:5619.
26. Mai J, Lachinov D, Riedl S, et al. Clinical validation for automated geographic atrophy monitoring on OCT under complement inhibitory treatment. *Sci Rep*. 2023;13:7028.
27. Sarks JP, Sarks SH, Killingsworth MC. Evolution of geographic atrophy of the retinal pigment epithelium. *Eye*. 1988;2:552–577.
28. Litts KM, Messinger JD, Dellatorre K, Yannuzzi LA, Freund KB, Curcio CA. Clinicopathological correlation of outer retinal tubulation in age-related macular degeneration. *JAMA Ophthalmol*. 2015;133:609–612.
29. Schaal KB, Freund KB, Litts KM, Zhang Y, Messinger JD, Curcio CA. Outer retinal tubulation in advanced age-related macular degeneration: optical coherence tomographic findings correspond to histology. *Retina*. 2015;35:1339–1350.
30. Reiter GS, Mai J, Riedl S, et al. AI in the clinical management of GA: a novel therapeutic universe requires novel tools. *Prog Ret Eye Res*. 2024;103:101305.
31. Wu Z, De Zanet S, Blair JPM, Guymer RH. Loss of OCT outer retinal bands as potential clinical trial endpoints in intermediate age-related macular degeneration. *Ophthalmol Sci*. 2025;5:100769.
32. Todorova V, Merolla L, Karademir D, et al. Retinal Layer Separation (ReLayS) method enables the molecular analysis of photoreceptor segments and cell bodies, as well as the inner retina. *Sci Rep*. 2022;12:20195.
33. Lindell M, Kar D, Sedova A, et al. Volumetric reconstruction of a human retinal pigment epithelial cell reveals specialized membranes and polarized distribution of organelles. *Invest Ophthalmol Vis Sci*. 2023;64:35.
34. Goerdt L, Swain TA, Kar D, et al. Band visibility in high-resolution optical coherence tomography assessed with a custom review tool and updated, histology-derived nomenclature. *Transl Vis Sci Tech*. 2024;13:19.
35. Zanzottera EC, Messinger JD, Ach T, Smith RT, Freund KB, Curcio CA. The Project MACULA retinal pigment epithelium grading system for histology and optical coherence tomography in age-related macular degeneration. *Invest Ophthalmol Vis Sci*. 2015;56:3253–3268.
36. Cao D, Leong B, Messinger JD, et al. Hyperreflective foci, OCT progression indicators in age-related macular degeneration, include transdifferentiated retinal pigment epithelium. *Invest Ophthalmol Vis Sci*. 2021;62:34.
37. Curcio CA, Messinger J, Berlin A, et al. Histology of fundus autofluorescence (FAF) in multifocal geographic atrophy (GA) with thick choroid in age-related macular degeneration (AMD). *Invest Ophthalmol Vis Sci*. 2024;65:2284–2284.
38. Edwards MM, McLeod DS, Bhutto IA, et al. Müller cell changes and subretinal membrane formation in an eye with multi-focal geographic atrophy. *medRXiv*. Preprint posted online February 3, 2026. https://doi.org/10.64898/2026.01.27.26344802.
39. McLeod DS, Bhutto IA, Messinger JD, et al. Choroidal vascular findings in a case of multifocal geographic atrophy: a clinicopathologic correlation. *Invest Ophthalmol Vis Sci*. 2026;67(3):19.
40. Li M, Huisingh C, Messinger JD, et al. Histology of geographic atrophy secondary to age-related macu-

lar degeneration: a multilayer approach. *Retina*. 2018; 38:1937–1953.
41. Li M, Dolz-Marco R, Huisingh C, et al. Clinicopathologic correlation of geographic atrophy secondary to age-related macular degeneration. *Retina*. 2019;39:802–816.
42. McLeod DS, Grebe R, Bhutto I, Merges C, Baba T, Lutty GA. Relationship between RPE and choriocapillaris in age-related macular degeneration. *Invest Ophthalmol Vis Sci*. 2009;50:4982–4991.
43. Vogt SD, Curcio CA, Wang L, et al. Retinal pigment epithelial expression of complement regulator CD46 is altered early in the course of geographic atrophy. *Exp Eye Res*. 2011;93:413–423.
44. Rudolf M, Vogt SD, Curcio CA, et al. Histologic basis of variations in retinal pigment epithelium autofluorescence in eyes with geographic atrophy. *Ophthalmology*. 2013;120:821–828.
45. Bird AC, Phillips RL, Hageman GS. Geographic atrophy: a histopathological assessment. *JAMA Ophthalmol*. 2014;132:338–345.
46. Eandi CM, Charles Messance H, Augustin S, et al. Subretinal mononuclear phagocytes induce cone segment loss via IL-1beta. *eLife* 2016;5:e16490.
47. Curcio CA, Kar D, Owsley C, Sloan KR, Ach T. Age-related macular degeneration, a mathematically tractable disease. *Invest Ophthalmol Vis Sci*. 2024;65:4.
48. Gundersen HJ. Stereology of arbitrary particles. A review of unbiased number and size estimators and the presentation of some new ones, in memory of William R. Thompson. *J Microsc*. 1986;143:3–45.
49. Schindelin J, Arganda-Carreras I, Frise E, et al. Fiji: an open-source platform for biological-image analysis. *Nat Methods*. 2012;9:676–682.
50. Brinkmann M, Bacci T, Kar D, et al. Histology and clinical lifecycle of acquired vitelliform lesion, a pathway to advanced age-related macular degeneration. *Am J Ophthalmol*. 2022;240:99–114.
51. Berlin A, Messinger JD, Ferrara D, Freund KB, Curcio CA. OCT features relevant to neovascular AMD management and non-neovascular AMD progression, a clinicopathologic correlation. *Ret Cases Brief Rep*. 2023;17:S41–S46.
52. Yiu G, Vuong VS, Oltjen S, et al. Effect of uveal melanocytes on choroidal morphology in rhesus macaques and humans on enhanced-depth imaging optical coherence tomography. *Invest Ophthalmol Vis Sci*. 2016;57:5764–5771.
53. Berlin A, Messinger JD, Ramtohul P, et al. Inflammatory cell activity in treated neovascular age-related macular degeneration, a histologic case study. *Retina*. 2023;43:1904–1913.
54. Spaide RF, Curcio CA. Drusen characterization with multimodal imaging. *Retina*. 2010;30:1441–1454.
55. Anderson DMG, Kotnala A, Migas L, et al. Lysolipids are prominent in subretinal drusenoid deposits, a high-risk phenotype in age-related macular degeneration. *Front Ophthalmol*. 2023;3:1258734.
56. Sarks SH. Ageing and degeneration in the macular region: a clinico-pathological study. *Br J Ophthalmol*. 1976;60:324–341.
57. Sarks S, Cherepanoff S, Killingsworth M, Sarks J. Relationship of basal laminar deposit and membranous debris to the clinical presentation of early age-related macular degeneration. *Invest Ophthalmol Vis Sci*. 2007;48:968–977.
58. Sura AA, Chen L, Messinger JD, et al. Measuring the contributions of basal laminar deposit and Bruch's membrane in age-related macular degeneration. *Invest Ophthalmol Vis Sci*. 2020;61:19.
59. van der Schaft TL, Mooy CM, de Bruijn WC, Oron FG, Mulder PGH, de Jong PTVM. Histologic features of the early stages of age-related macular degeneration. *Ophthalmology*. 1992;99:278–286.
60. van der Schaft TL, de Bruijn WC, Mooy CM, de Jong PTVM. Basal laminar deposit in the aging peripheral human retina. *Graefes Arch Clin Exp Ophthalmol*. 1993;231:470–475.
61. Rudolf M, Clark ME, Chimento M, Li C-M, Medeiros NE, Curcio CA. Prevalence and morphology of druse types in the macula and periphery of eyes with age-related maculopathy. *Invest Ophthalmol Vis Sci*. 2008;49:1200–1209.
62. Lindblad AS, Lloyd PC, Clemons TE, et al. Change in area of geographic atrophy in the Age-Related Eye Disease Study: AREDS report number 26. *Arch Ophthalmol*. 2009;127:1168–1174.
63. Bellmann C, Jorzik J, Spital G, Unnebrink K, Pauleikhoff D, Holz FG. Symmetry of bilateral lesions in geographic atrophy in patients with age-related macular degeneration. *Arch Ophthalmol*. 2002;120:579–584.
64. Trivizki O, Wang L, Shi Y, et al. Symmetry of macular fundus features in age-related macular degeneration. *Ophthalmol Retina*. 2023;7:672–682.
65. Keenan TD, Agron E, Domalpally A, et al. Progression of geographic atrophy in age-related macular degeneration: AREDS2 Report Number 16. *Ophthalmology*. 2018;125:1913–1928.
66. Colijn JM, Liefers B, Joachim N, et al. Enlargement of geographic atrophy from first diagnosis to end of life. *JAMA Ophthalmol*. 2021;139:743–750.
67. Takahashi A, Ooto S, Yamashiro K, et al. Pachychoroid geographic atrophy: clinical and genetic characteristics. *Ophthalmol Retina*. 2018;2:295–305.
68. Sato Y, Ueda-Arakawa N, Takahashi A, et al. Clinical characteristics and progression of pachychoroid and conventional geographic atrophy. *Ophthalmol Sci*. 2024;4:100528.
69. Dolz-Marco R, Gal-Or O, Freund KB. Choroidal thickness influences near-infrared reflectance intensity in eyes with geographic atrophy due to age-related macular degeneration. *Invest Ophthalmol Vis Sci*. 2016;57:6440–6446.
70. Thiele S, Pfau M, Larsen PP, Fleckenstein M, Holz FG, Schmitz-Valckenberg S. Multimodal imaging patterns for development of central atrophy secondary to age-related macular degeneration. *Invest Ophthalmol Vis Sci*. 2018;59:AMD1–AMD11.
71. Yordi S, Cakir Y, Kalra G, et al. Ellipsoid zone integrity and visual function in dry age-related macular degeneration. *J Pers Med*. 2024;14:543.
72. Fu DJ, Bagga P, Naik G, et al. Pegcetacoplan treatment and consensus features of geographic atrophy over 24 months. *JAMA Ophthalmol*. 2024;142:548–558.
73. Masri RA, Greferath U, Fletcher EL, Martin PR, Grunert U. Immunohistochemistry and spatial density of Muller cells in the human fovea. *Invest Ophthalmol Vis Sci*. 2025;66:46.
74. Greferath U, Guymer RH, Vessey KA, Brassington K, Fletcher EL. Correlation of histologic features with in vivo imaging of reticular pseudodrusen. *Ophthalmology*. 2016;123:1320–1331.
75. Shen LL, Sun M, Grossetta Nardini HK, Del Priore LV. Progression of unifocal versus multifocal geographic atrophy in age-related macular degeneration: a systematic review and meta-analysis. *Ophthalmol Retina*. 2020;4:899–910.
76. Shen LL, Sun M, Ahluwalia A, Young BK, Park MM, Del Priore LV. Geographic atrophy growth is strongly related to lesion perimeter: unifying effects of lesion area, number, and circularity on growth. *Ophthalmol Retina*. 2021;5:868–878.
77. Pfau M, Lindner M, Goerdt L, et al. Prognostic value of shape-descriptive factors for the progression of geographic

Investigative Ophthalmology & Visual Science

atrophy secondary to age-related macular degeneration. *Retina*. 2019;39:1527–1540.
78. Suzuki M, Curcio CA, Mullins RF, Spaide RF. Refractile drusen: clinical imaging and candidate histology. *Retina*. 2015;35:859–865.
79. Tan AC, Pilgrim M, Fearn S, et al. Calcified nodules in retinal drusen are associated with disease progression with age-related macular degeneration. *Sci Transl Med*. 2018;10:466–477.
80. Chen L, Messinger JD, Ferrara D, Freund KB, Curcio CA. Stages of drusen-associated atrophy in age-related macular degeneration visible via histologically validated fundus autofluorescence. *Ophthalmol Retina*. 2021;5:730–742.
81. Litts KM, Messinger JD, Zhang Y, Freund KB, Curcio CA. Inner segment remodeling and mitochondrial translocation in degenerating cones of age-related macular degeneration, including outer retinal tubulation. *Invest Ophthalmol Vis Sci*. 2015;56:2243–2253.
82. Dunaief JL, Dentchev T, Ying GS, Milam AH. The role of apoptosis in age-related macular degeneration. *Arch Ophthalmol*. 2002;120:1435–1442.
83. Pfau M, von der Emde L, de Sisternes L, et al. Progression of photoreceptor degeneration in geographic atrophy secondary to age-related macular degeneration. *JAMA Ophthalmol*. 2020;138:1026–1034.
84. Mitamura Y, Mitamura-Aizawa S, Katome T, et al. Photoreceptor impairment and restoration on optical coherence tomographic image. *J Ophthalmol*. 2013;2013:518170.
85. Collin GB, Gogna N, Chang B, et al. Mouse models of inherited retinal degeneration with photoreceptor cell loss. *Cells* 2020;9:931.
86. Li JD, Govardovskii VI, Steinberg RH. Light-dependent hydration of the space surrounding photoreceptors in the cat retina. *Vis Neurosci*. 1994;11:743–752.
87. Bissig D, Berkowitz BA. Light-dependent changes in outer retinal water diffusion in rats in vivo. *Mol Vis*. 2012;18:2561–2577.
88. Berkowitz BA, Podolsky RH, Childers KL, et al. Functional changes within the rod inner segment ellipsoid in wild-type mice: an optical coherence tomography and electron microscopy study. *Invest Ophthalmol Vis Sci*. 2022;63:8.
89. Ishikawa M, Sawada Y, Yoshitomi T. Structure and function of the interphotoreceptor matrix surrounding retinal photoreceptor cells. *Exp Eye Res*. 2015;133:3–18.
90. Uehara F, Matthes MT, Yasumura D, LaVail MM. Light-evoked changes in the interphotoreceptor matrix. *Science*. 1990;248:1633–1636.
91. Yokomizo H, Maeda Y, Park K, et al. Retinol binding protein 3 is increased in the retina of patients with diabetes resistant to diabetic retinopathy. *Sci Transl Med*. 2019;11(499):eaau6627.
92. Berkowitz BA. Preventing diabetic retinopathy by mitigating subretinal space oxidative stress in vivo. *Vis Neurosci*. 2020;37:E002.
93. Panorgias A, Zawadzki RJ, Capps AG, Hunter AA, Morse LS, Werner JS. Multimodal assessment of microscopic morphology and retinal function in patients with geographic atrophy. *Invest Ophthalmol Vis Sci*. 2013;54:4372–4384.
94. Brar M, Kozak I, Cheng L, et al. Correlation between spectral-domain optical coherence tomography and fundus autofluorescence at the margins of geographic atrophy. *Am J Ophthalmol*. 2009;148:439–444.
95. Fleckenstein M, Schmitz-Valckenberg S, Martens C, et al. Fundus autofluorescence and spectral domain optical coherence tomography characteristics in a rapidly progressing form of geographic atrophy. *Invest Ophthalmol Vis Sci*. 2011;52:3761–3766.
96. Sayegh RG, Simader C, Scheschy U, et al. A systematic comparison of spectral-domain optical coherence tomography and fundus autofluorescence in patients with geographic atrophy. *Ophthalmology*. 2011;118:1844–1851.
97. Schmitz-Valckenberg S, Fleckenstein M, Gobel AP, Hohman TC, Holz FG. Optical coherence tomography and autofluorescence findings in areas with geographic atrophy due to age-related macular degeneration. *Invest Ophthalmol Vis Sci*. 2011;51:1–6.
98. Abdillahi H, Enzmann V, Wittwer VV, Wolf S, UE Wolf-Schnurrbusch. Vitreoretinal interface changes in geographic atrophy. *Ophthalmology*. 2014;121:1734–1739.
99. Yehoshua Z, de Amorim Garcia Filho CA, Nunes RP, et al. Comparison of geographic atrophy growth rates using different imaging modalities in the COMPLETE Study. *Ophthalmic Surg Lasers Imaging Retina*. 2015;46:413–422.
100. Qu J, Velaga SB, Hariri AH, Nittala MG, Sadda S. Classification and quantitative analysis of geographic atrophy junctional zone using spectral domain optical coherence tomography. *Retina*. 2018;38:1456–1463.
101. Mahmoudi A, Corradetti G, Emamverdi M, et al. Atrophic lesions associated with age-related macular degeneration: high-resolution versus standard OCT. *Ophthalmol Retina*. 2024;8:367–375.
102. Sadda S, Hatcher KA, Shah BK, Kondapalli SS, Li C, Baumal CR. Outer retinal tubulation and geographic atrophy: a natural history analysis of sham observed eyes from the OAKS and DERBY trials. *Ophthalmol Ther*. 2025;14:1611–1619.
103. Wilson JD, Foster TH. Mie theory interpretations of light scattering from intact cells. *Opt Lett*. 2005;30:2442–2444.
104. Wilson JD, Cottrell WJ, Foster TH. Index-of-refraction-dependent subcellular light scattering observed with organelle-specific dyes. *J Biomed Optics*. 2007;12:014010.
105. Wilson JD, Foster TH. Characterization of lysosomal contribution to whole-cell light scattering by organelle ablation. *J Biomed Optics*. 2007;12:030503.
106. Curcio CA, Medeiros NE, Millican CL. Photoreceptor loss in age-related macular degeneration. *Invest Ophthalmol Vis Sci*. 1996;37:1236–1249.
107. Litts KM, Wang X, Clark ME, et al. Exploring photoreceptor reflectivity via multimodal imaging of outer retinal tubulation in advanced age-related macular degeneration. *Retina*. 2017;37:978–988.
108. Dolz-Marco R, Litts KM, Tan ACS, Freund KB, Curcio CA. The evolution of outer retinal tubulation, a neurodegeneration and gliosis prominent in macular diseases. *Ophthalmology*. 2017;124:1353–1367.
109. Preti RC, Govetto A, Filho RGA, et al. Optical coherence tomography analysis of outer retinal tubulations: sequential evolution and pathophysiological insights. *Retina*. 2017;38:1518–1525.
110. Youle RJ, van der Bliek AM. Mitochondrial fission, fusion, and stress. *Science*. 2012;337:1062–1065.
111. Hayes MJ, Tracey-White D, Kam JH, Powner MB, Jeffery G. The 3D organisation of mitochondria in primate photoreceptors. *Sci Rep*. 2021;11:18863.
112. Allingham MJ, Mettu PS, Cousins SW. Phase 1 clinical trial of elamipretide in intermediate age-related macular degeneration and high-risk drusen: ReCLAIM High-Risk Drusen Study. *Ophthalmol Sci*. 2022;2:100095.
113. Boyer D, Hu A, Warrow D, et al. LIGHTSITE III: 13-month efficacy and safety evaluation of multiwavelength photobiomodulation in nonexudative (dry) age-related macular degeneration using the Lumithera Valeda Light Delivery System. *Retina*. 2024;44:487–497.

Investigative Ophthalmology & Visual Science

114. Pfau M, Emde LV, Dysli C, et al. Determinants of cone- and rod-function in geographic atrophy: AI-based structure-function correlation. *Am J Ophthalmol*. 2020;217:162–173.
115. Moult EM, Waheed NK, Novais EA, et al. Swept-source optical coherence tomography angiography reveals choriocapillaris alterations in eyes with nascent geographic atrophy and drusen-associated geographic atrophy. *Retina*. 2016;36(1):S2–S11.
116. Kvanta A, Casselholm de Salles M, Amren U, Bartuma H. Optical coherence tomography angiography of the foveal microvasculature in geographic atrophy. *Retina*. 2017;37:936–942.
117. Sacconi R, Corbelli E, Carnevali A, Querques L, Bandello F, Querques G. Optical coherence tomography angiography in geographic atrophy. *Retina*. 2017;38:2350–2355.
118. Nassisi M, Shi Y, Fan W, et al. Choriocapillaris impairment around the atrophic lesions in patients with geographic atrophy: a swept-source optical coherence tomography angiography study. *Br J Ophthalmol*. 2018;103:911–917.
119. Sacconi R, Corbelli E, Borrelli E, et al. Choriocapillaris flow impairment could predict the enlargement of geographic atrophy lesion. *Br J Ophthalmol*. 2021;105:97–102.
120. Nassisi M, Baghdasaryan E, Tepelus T, Asanad S, Borrelli E, Sadda SR. Topographic distribution of choriocapillaris flow deficits in healthy eyes. *PLoS ONE*. 2018;13:e0207638.
121. Zheng F, Zhang Q, Shi Y, et al. Age-dependent changes in the macular choriocapillaris of normal eyes imaged with swept-source OCT angiography. *Am J Ophthalmol*. 2019;200:110–122.
122. Ramrattan RS, van der Schaft TL, Mooy CM, de Bruijn WC, Mulder PGH, de Jong PTVM. Morphometric analysis of Bruch's membrane, the choriocapillaris, and the choroid in aging. *Invest Ophthalmol Vis Sci*. 1994;35:2857–2864.
123. Mullins RF, Johnson MN, Faidley EA, Skeie JM, Huang J. Choriocapillaris vascular dropout related to density of drusen in human eyes with early age-related macular degeneration. *Invest Ophthalmol Vis Sci*. 2011;52:1606–1612.
124. Grebe R, Mughal I, Bryden W, et al. Ultrastructural analysis of submacular choriocapillaris and its transport systems in AMD and aged control eyes. *Exp Eye Res*. 2019;181:252–262.

Investigative Ophthalmology & Visual Science